RAIN GENERATED RING-WAVES: MEASUREMENTS AND MODELING FOR REMOTE SENSING

LARRY F. BLIVEN
NASA/Goddard Space Flight Center
Laboratory for Hydrospheric Processes
Wallops Island, VA 23337 USA

PIOTR W. SOBIESKI and CHRISTOPHE CRAEYE
Université Catholique de Louvain
Laboratoire de Télécommunications et Télédetection
pl. du Levant, 2
B-1348 Louvain-la-Neuve, Belgium

The *International Journal of Remote Sensing*,
Vol 18, No. 1, 221-228.

Homepage: bliven2.osb.wff.nasa.gov
Email: bliven@osb.wff.nasa.gov
Office Phone:757-824-1057

1. Introduction

This article addresses measurement and modeling of rain generated ring-waves on water surfaces, which contributes to developing numerical models for quantitative assessment of radar returns from rain roughened seas. Remote sensing offers the potential for improved estimates of rain in oceanic regions, and those observations will be useful for weather and climate studies because rain is a major factor in heat and moisture fluxes (Simpson 1988, Peixoto and Oort 1992). Development of innovative sensors and reliable data inversion algorithms will be expedited by understanding radar scattering from rain roughened water surfaces.

What are the major splash products from rain roughened water surfaces that influence radar scattering? Photographs by Worthington (1882) show that when a water drop hits a water surface, it can generate a cavity with a crown, which collapses to form a vertical stalk of water, which subsides to spawn rings of gravity-capillary waves that propagate outward. Laboratory data show that backscattered power from splash products is attributable to stalks (Wetzel, 1990) and to ring-waves (Bliven *et al.* 1993a, Sobieski and Bliven 1995). The former is the dominant scattering feature for radars viewing at grazing angles, and the latter is the dominant scattering feature at 30^{o} incidence angle. Both stalk and ring-wave distributions are important for a universal model, however model development can be simplified by examining each separately. Because satellite-borne sensors usually view the ocean at angles closer to 30^{o} incidence angle than to grazing, we decided to commence by measuring ring-waves and by modeling ring-wave wavenumber spectra, which is the form used in many radar scattering models.

Rain drops strike water surfaces at nearly terminal velocity, so ring-wave spectra should be measured for similar conditions. *In situ* measurements of rain rates, drop size distributions, water surface morphology and radar data would be ideal, but those data are not available and their measurement presents the usual logistical problems associated with rain studies. Therefore we conducted experiments in a tower so that simulated rain drops impact the water surface at terminal velocity. Hence we systematically obtained ring-wave and scatterometer data for simulated rain rates of 5 to 200 mm hr^{-1}. The experimental setting is described in section 2, analysis of the data is presented in section 3, and we close with a summary.

2. Experimental Setting

We conducted the experiments at the NASA Wallops Flight Facility in the Rain-Sea Interaction Facility (RSIF), which is the 4 x 4 x 17 m tower that is part of the N-159 aircraft hangar. The distinctive dimension is the 17 m height that is sufficient for droplets released from the overhead catwalk level to approach terminal velocity near ground level. Rain simulations in wind-wave tanks typically have drop fall distances of about 1 m, so drop sizes of interest impact the water surface at speeds much less than terminal velocity. On the other hand, the speed of 2.8 mm drops that fall 13 m in the RSIF was measured to be 7.8 m s^{-1} (Sobieski and Bliven 1995), which is within 1 % of terminal velocity (Gunn and Kinzer 1949).

Simulated rain is from a 80 x 80 x 6 cm stainless steel box and its bottom has 1100 holes that are separated by 2.5 cm between center points. Each hole holds a plastic nipple, to which hypodermic needles can be temporarily attached to create water drops with diameters from 1.2 to 4.2 mm. For these experiments, we used gauge 20 needles that produce 2.8 mm water droplets, which is close to the median size for natural rains. The close nozzle spacing permits rainfall rates up to 200 mm hr^{-1} with 2.8 mm drops at an average drip rate less than 2 Hz from the nozzles.

This provides unambiguous identification of ring-waves in surface-elevation frequency spectra because the drip frequency is lower than ring-wave frequencies. We hoisted the simulator with a winch and attached it to the cat-walk. It was centered above the tank, so drops fell 13 m before striking the water surface at terminal velocity.

For each series of observations, the 2 x 1 x 1 m tank was cleaned and filled with fresh water to a depth of 80 cm. Sobieski and Bliven (1995) examined scatterometer returns from single drop impacts on both fresh and saline water; the results are similar. So we begin with fresh water experiments and experiments with saline water can be conducted in the future. We use a capacitance probe to measure elevation time-series. For further information concerning the capacitance probe, see Strum and Sorrell (1973), Bliven *et al*. (1986), and Long (1992). For this study, the small wire sensor penetrated the water surface adjacent to the rain footprint in the tank. The system provides an analog voltage that is linearly related to surface elevation relative to the mean water level. Because craters, crowns and stalks do not propagate, the capacitance probe measured only the desired feature -waves. To measure radar cross sections, we operated a 13.5 GHz scatterometer at 30^{o} inclination from nadir and with vertical polarization, as in Bliven and Giovanangeli (1993) and Bliven *et al*. (1993 a&b). It pointed towards the center of the rain footprint on the water surface. We computed normalized radar cross sections by dividing the data by the backscattered power from a 15 cm sphere at the operational range.

3. Results

The following results are derived from 10 series of experiments with rain rates from 5 to 200 mm hr^{-1}. For each series, data were obtained for 39 rain rates by using a computer controlled pump to regulate the volume flow rate of filtered water into the rain simulator. The pump changed flow rates every five minutes, and the data acquisition system was synchronized with it, (three minutes for settling, two minutes for data). Even for extreme changes in flow rates, adjustment to new conditions takes less than three minutes. The 39 cases were logarithmically spaced from 5 to 200 mm hr^{-1}, and either a sequential or a random sequence was run for each series.

3.1. Frequency spectra of the dominant ring-waves: S_f

Frequency spectra of surface elevation were computed from 20 minutes of capacitance probe data for each rain rate, and examples are displayed in Figure 1a. Spectral resolution is 0.25 Hz. The dominant energy containing portion of the spectra is the interval from 3.25 to 12 Hz, which contains about 90% of the total variance of surface elevation. We refer to waves in this interval as the dominant ring-waves. Notice that the dominant ring-wave spectra $S_f(mm^2\ Hz^{-1})$ have a similar shape, *i.e.* the maxima occur at almost the same frequency, the bandwidths are comparable, and the roll-offs are asymmetric with the low frequency side decaying faster than the high frequency tail.

To characterize the frequency spectra of the dominant ring-waves, we choose a log-Gaussian model of the form

$$S_f(f) = S_{fp}(R) \exp\left\{ -\Pi \left[\frac{\ln\left(\frac{f}{f_p}\right)}{\frac{\Delta f}{f_p}} \right]^2 \right\} . \qquad (1)$$

S_{fp} is the amplitude of the spectral peak, f_p is the frequency at the peak and Δf is the bandwidth. For each rain intensity, the coefficients were computed by using a least squares algorithm.

Let's examine the spectral shape first. For the 39 cases, f_p(Hz) = 5.772 - 0.0018 R(mm hr^{-1}) and Δf(Hz) = 4.42 + 0.0028 R(mm hr^{-1}), with r^2 = 0.80 and 0.86 respectively. The peak frequency and bandwidth are practically independent of R, i.e. f_p(Hz) = 5.68 ± 0.12 and Δf(Hz) = 4.57 ± 0.18. For some applications it is essential to use the complete log-Gaussian model with an R dependent shape factor. On the other hand, the average shape is well represented by the log-Gaussian model with f_p = 5.68 Hz and Δf = 4.57 Hz. To show this, we normalized each elevation spectrum by its variance, and computed the average normalized spectrum ψ_f(Hz^{-1}) for all rain rates that is displayed in Figure 1b. The similarity between the shape of the average log-Gaussian model and the shape of ψ_f is apparent ($r^2 > 0.98$).

How does the amplitude of the rain roughened surface vary with respect to R? Surface roughness increases as R increases, as shown in Figure 2a which displays surface elevation variance η^2(R). The slope of η^2(R) decreases as R increases, so the linear representation proposed by Bliven *et al*. (1993a) for light rains (R < 30 mm hr^{-1}) is not fitting for this broad range of observations. A power law model provides good agreement with the data, and a least-squares regression yields

$$\eta^2(mm^2) = 0.25\, R^{0.59}\ (mm\ hr^{-1}) , \qquad (2)$$

Likewise the amplitude of the dominant ring-waves increases as R increases; see Figure 2b, and the power law model is

$$S_{fp}(mm^2\ hz^{-1}) = 0.060\, R^{0.53}\ (mm\ hr^{-1}) . \qquad (3)$$

Although the spectral shapes are quite similar, the exponents of Eqs. 2 and 3 are slightly different, so η^2 and S_{fp} are not linearly related. Both f_p and Δf are weak functions of R and the spectral model is constructed using a fixed frequency band, rather than a variable bandwidth that contains a fixed fraction of the total variance, so we attribute some of the difference to systematic variability of the spectral shape.

Rain generates not only ring-waves on the water surface but also turbulence beneath the water surface. Turbulence interacts with ring-waves to cause their attenuation. The generation, interaction and dissipation processes need further measurement and explanation in order to understand their roles in $S_{fp}(R)$; so it is too soon to offer a quantitative physical explanation of a particular model form or its coefficients. We merely describe $S_{fp}(R)$ using an empirical model.

Analysis of the frequency spectra of ring-waves reveals (a) that the spectral magnitude is a nonlinear function of R and (b) that the spectral shape is practically constant and it is well represented by a log-Gaussian model.

3.2. Wavenumber spectra of ring-waves: S_k

Wavenumber spectra of ring-waves are derived from frequency spectra by using a dispersion relationship that depends upon the fluid properties and wave characteristics. A suitable dispersion relationship for gravity-capillary waves is

$$\sigma^2 = g\,k + \frac{\tau}{\rho}\,k^3 , \qquad (4)$$

where k, σ, g, ρ and τ are the wavenumber (cm^{-1}), radian frequency ($rd\ s^{-1}$), the gravitational constant, density of water and water surface tension (~74 dynes cm^{-1}). The change of variables between frequency space and wavenumber space is accomplished with the following formula

$$S_k(k) = \frac{1}{2\pi} S_f(f(k)) \frac{d\sigma}{dk} , \qquad (5)$$

where the derivative of radian frequency with respect to wavenumber is the group velocity C_g. Thus equation 1 yields the following log-Gaussian wavenumber spectral model

$$S_k(k) = \frac{1}{2\pi}\, C_g(k)\; S_{fp} \exp\left\{ -\pi \left[\frac{\ln\left(\frac{\sqrt{gk + \frac{\tau}{\rho}k^3}}{2\pi f_p} \right)}{\frac{\Delta f}{f_p}} \right]^2 \right\} . \qquad (6)$$

The shape of the normalized log-Gaussian wavenumber spectral model ψ_k(rd^{-1} cm) is depicted in Figure 3, for which f_p = 5.68 Hz and Δf = 4.57 Hz. Wavelength λ is related to wavenumber as λ = 2 pi/k. Hence ring-wave energy is mainly attributable to wavelengths ranging from 2 to 15 cm, with the maximum near 5.3 cm.

The log-Gaussian wavenumber spectral representation for ring-waves was first promoted by Sobieski (1991), who conceived it for natural rains from the theoretical analysis of single drop impacts by Le Méhauté (1988). These results show that a log-Gaussian wavenumber representation is suitable for modeling ring-waves.

3.3. Scatterometer Response

During the experiments, scatterometric data were obtained from the 13.5 GHz scatterometer (30^o incidence angle, vertical polarization) and average normalized radar cross sections (NRC) were computed from the 20 minutes of data for each rain rate. The results are displayed in Figure 4, which shows that the following power law model closely conforms to the data.

$$NRC = 0.084\ R^{0.46}(mm\ \ hr^{-1})\ . \qquad (7)$$

Spectral shape factors ($f_p(R)$ and $\Delta f(R)$) contribute to some of the difference between the power law exponents in equations 3 and 7. Therefore to examine more closely the relationship between the ring-wave spectra and NRC, we computed the correlation between NRC values and ring-wave spectral densities close to the Bragg resonance wavelength. For this computation we used the spectral band corresponding to wavelengths between 1.98 and 2.03 cm. The correlation coefficient for a linear model is greater than 0.97, so the Bragg scattering process is tenable for the full range of simulated rains.

4. Conclusion

This data analysis provides a quantitative basis for characterizing ring wave spectra for simulated rains rates up to 200 mm hr^{-1}. The experimental conditions in the Rain-Sea Interaction Facility consisted of a water surface that was agitated by 2.8 mm water droplets that accelerated to terminal velocity before impact. Ring-wave energy is predominately within the range of wavelengths from 2 to 15 cm, with the maximum at about 5.3 cm. Frequency spectra and wavenumber spectra are well represented by log-Gaussian spectral models. Ring-wave energy and backscattered power from a 13.5 GHz scatterometer increase as R increases, but the growth rates slacken at higher rain intensities.

For light rains ($R < 30$ mm hr^{-1}), Bliven *et al*. (1993a) proposed a linear relationship for ring-wave growth. A plausible explanation for the reduced growth rates at higher rain rates is that enhancement of rain generated turbulence in the boundary layer increases ring-wave dissipation. Yet for the higher rain rates in this study, both ring-wave magnitude and NRC(R) increase monotonically, which implies that the turbulence intensities were not sufficient to quell the ring-waves. To see if ring-waves approach a 'saturation' limit or if turbulence eventually 'calms' ring-waves, data are needed (a) for extremely high rain rates and (b) for larger drops that generate turbulence more effectively.

The results from this study can be used to guide scattering model development because the log-Gaussian wavenumber spectral model of ring-waves can be incorporated into numerical scattering models, such as the one described by Guissard *et al*. (1994) and Sobieski *et al*. (1994), and the scatterometer data can be used to assess the simulations. For stratiform rains and large sample populations, the negative-exponential drop size distribution model of Marshall and Palmer (1948) is quite representative. For the range of simulated rains in these laboratory experiments, the kinetic energy flux is within a factor of two of the kinetic energy flux of natural rains that have Marshall-Palmer drop size distributions. Additional data will be needed to ensure that a comprehensive description of rain-roughened sea morphology emerges, and measurements from natural settings will help the evolution to robust models. Unquestionably the influence of drop size distribution on ring-wave generation needs to be addressed; and so do the attenuation

effects of rain generated turbulence on ring-waves and on wind-waves. We believe that these are the main issues to be dealt with in order to progress towards understanding radar scattering from rain roughened seas.

Acknowledgments
Financial support was provided by the NASA Mission to Planet Earth Program through the RTOP 972-461-31-08, the Scientific Development Fund of UCL and the Belgian National Research Fund (National Lottery).

References

BLIVEN, L. and GIOVANANGELI, J-P., 1993, An experimental study of microwave scattering from rain- and wind-roughened seas. *International Journal of Remote Sensing*, **14(5)**, 855-869.

BLIVEN, L., BRANGER, H., SOBIESKI, P. and GIOVANANGELI, J-P., 1993a, An analysis of scatterometer returns from a water surface agitated by artificial rain: evidence that ring-waves are the main feature. *International Journal of Remote Sensing*, **14(12)**, 2315-2329.

BLIVEN, L., GIOVANANGELI, J-P., WANNINKHOF, R.W. and CHAPRON, B., 1993b, A laboratory study of friction velocity estimates from scatterometry: low and high regimes. *International Journal of Remote Sensing*, **14(9)**, 1775-1785.

BLIVEN, L.F., HUANG, N.E. and LONG, S.R., 1986, Experimental study of the influence of wind on Benjamin-Feir sideband instability. *Journal of Fluid Mechanics*, **162**, 237-260.

GUISSARD, A., BAUFAYS, C. and SOBIESKI, P., 1994, Fully and nonfully developed sea models for microwave remote sensing applications. *Remote Sensing of the Environment*, **48**, 25-38.

GUNN, R. and KINZER, G.D., 1949, The terminal velocities of fall for water droplets in stagnant air. *Journal of Meteorology*, **6**, 243-248.

LE MEHAUTE, B., 1988, Gravity-capillary rings generated by water drops. *Journal of Fluid Mechanics*, **197**, 415-427.

LONG, S.R., 1992, A self-zeroing capacitance probe for water wave measurements. *NASA Reference Publication 1278*, NASA, Wallops Island, VA, 52 p.

MARSHAL, J.S. and PALMER, W.M.K., 1948, The distribution of raindrops with size. *Journal of Meteorology*, **6**, 165-166.

PEIXOTO, J.P. and OORT, A.H., 1992, **Physics of Climate**, American Institute of Physics, New York, NY.

SIMPSON J. (ed) 1988, Report of the science steering group for a Tropical Rainfall Measuring Mission (TRMM). *NASA Reference Publication 1-94*, NASA\GSFC, Greenbelt, MD, 94 p.

SOBIESKI, P., 1991, Personal communication.

SOBIESKI, P. and BLIVEN, L.F., 1995, Analysis of High Speed Images of Raindrop Splash Products and Ku-band Scatterometer Returns. *International Journal of Remote Sensing*, **16(14),** 2721-2726.

SOBIESKI, P., GUISSARD, A. and BAUFAYS, C., 1994, Comparison of microwave signatures for fully and nonfully developed sea models. *Remote Sensing of the Environment*, **48**, 39-50.

STRUM, G.V. and SORRELL, F.Y., 1973, Optical wave measurement technique and experimental comparison with wave height probes. *Applied Optics*, **12**, 1928-1933.

WETZEL, L.B., 1990, On the theory of electromagnetic scattering from a raindrop splash. *Radio Science*, **25(6)**, 1183-1197.

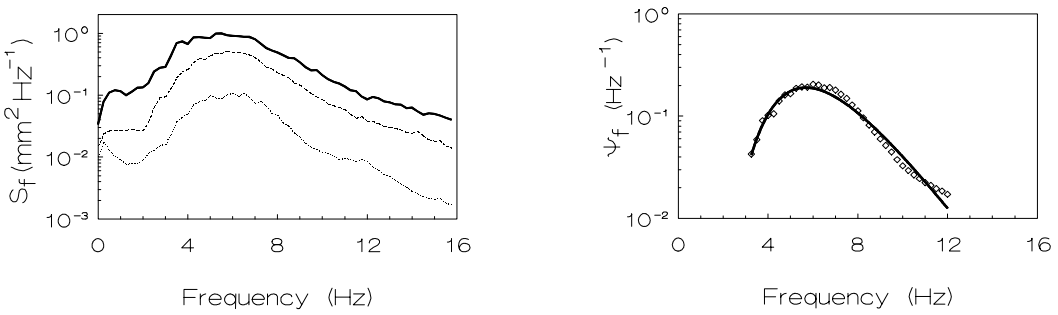

Figure 1. Ring-wave frequency spectra S_f show that the water surface becomes rougher as R increases, that the spectra have a similar shape and that the frequency range of 3.25 to 12 Hz contains most of the variance; the subplot shows S_f for R = 5, 50 and 200 mm hr^{-1} as dots, dashes, line. The normalized log-Gaussian spectral model with f_p = 5.68 Hz and Δf = 4.57 Hz is in close agreement with the average normalized frequency spectrum ψ_f (◊).

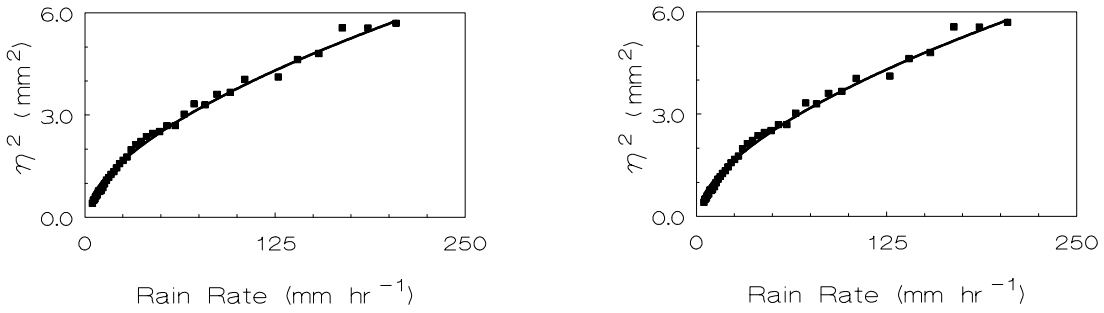

Figure 2. The elevation variance (■) and the spectral magnitude S_{fp} (▽) are well represented by the power law models presented in equations 2 & 3.

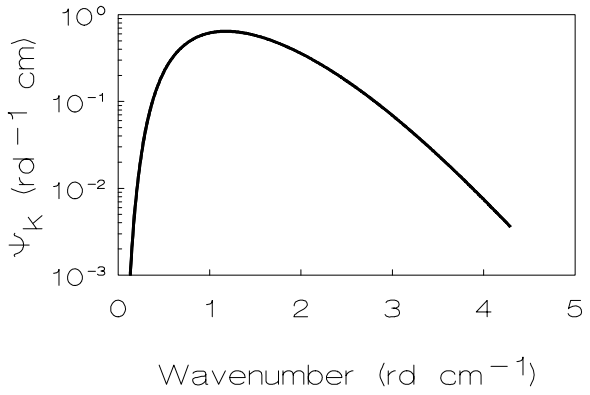

Figure 3. The normalized log-Gaussian wavenumber spectrum ψ_k shows that the dominant energy is from ring-waves with wavelengths of 2 to 15 cm and that the peak is at about 5.3 cm wavelength.

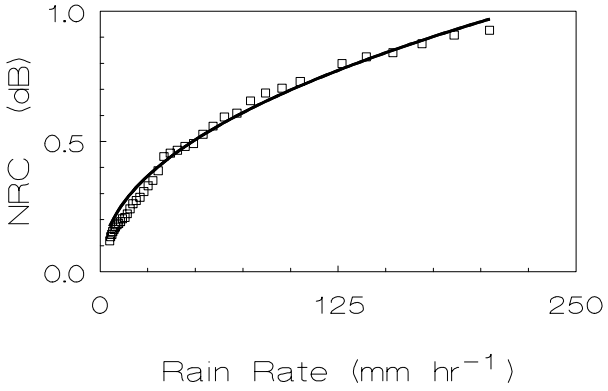

Figure 4. NRC from the Ku-band scatterometer data (□) is represented well by the power-law model of equation 7.